


# Impact of a Multi-step Heat Treatment on Different Manufacturing Routes of 18CrNiMo7-6 Steel



PARANJAYEE MANDAL , MAIDER OLASOLO, LAURIE DA SILVA,  
and HIMANSHU LALVANI

Effect of an optimized multi-step heat treatment routine on conventional (machining from wrought bar stock) and alternate manufacturing routes (hot forging and cold rotary forging) for producing flat cylindrical-shaped machine drive components from 18CrNiMo7-6 steel was investigated. The microstructure and mechanical properties of the final component manufactured using these three different routes were analyzed using optical microscopy, electron backscatter diffraction (EBSD), hardness testing, electro-thermal mechanical testing (ETMT), and rotary bending fatigue testing (RBFT) before and after implementing the multi-step heat treatment. It was found that the multi-step heat treatment transformed the as-received microstructure into the tempered martensitic microstructure, improving hardness, tensile, and fatigue properties. The heat treatment produced desired properties for the components manufactured by all three different routes. However the cold rotary forging, which is the most material utilizing route over the others, benefited the most from the optimized heat treatment.

<https://doi.org/10.1007/s11661-020-05728-x>  
© The Author(s) 2020

## I. INTRODUCTION

THE case-hardened 18CrNiMo7-6 steel is widely used in the field of transportation, energy generation, and general mechanical engineering due to its three key characteristics—high wear resistance, good fatigue strength, and cost-efficiency. The typical applications include gears of all kinds, camshafts, heavy-duty axles and arbors, bushings, wear pins, bearings, sprockets, metal rolling equipment, machine tools, universal joints, link components, *etc.*<sup>[1,2]</sup> This steel is typically supplied in the annealed condition followed by a multi-step heat treatment that develops a hard wear-resistant case (hardness of up to 60 HRC) on a relatively soft core material. Alloying the base material with chromium, molybdenum or nickel enhances the hardenability and impact toughness of the core material, whereas the quenching and tempering treatments increase the strength of core material by developing a martensitic microstructure. Additionally, the heat treatment can be

selected in such a way that it imparts a homogenous microstructure with fine grain size in the core material. This microstructural homogeneity of any case-hardened steels is affected by macro-segregation and micro-segregation. Macro-segregation occurs due to the difference in chemical composition in the material, whereas micro-segregation appears because of the difference between the alloying elements during the solidification process.<sup>[3,4]</sup> During heat treatment, the micro-segregated areas respond differently and often transform into different phases depending on the heat treatment and cooling rate. For example, austenization followed by slow cooling of low and medium carbon steels results in micro-segregation during solidification, *i.e.*, forms a banded microstructure consisted of alternating areas of ferrite and pearlite. Micro-segregation can also be observed in the carburized layer in alternating areas of martensite and bainite or of retained austenite and martensite depending on the chemical composition of the steel and the cooling rate. Both retained austenite and bainite are much softer than martensite, thus the banded microstructure shows large differences in strength and hardness along the longitudinal and transverse directions.<sup>[3]</sup> Grain size is another important factor influencing the core properties. Forging often develops large grains and unwanted structural components such as bainite and carbides in the steel microstructure due to overheating that adversely influences the impact strength, fatigue strength, and machinability. Normalizing is a commonly used heat treatment to obtain a fine-grain homogeneous microstructure with

---

PARANJAYEE MANDAL, LAURIE DA SILVA, and HIMANSHU LALVANI are with the Advanced Forming Research Centre, University of Strathclyde, 85 Inchinnan Drive, Inchinnan, Renfrew PA4 9LJ, UK. MAIDER OLASOLO is with the Advanced Forming Research Centre, University of Strathclyde, 85 Inchinnan Drive, Inchinnan, Renfrew PA4 9LJ, UK and also with the Advanced Materials Research Laboratory, University of Strathclyde, 75 Montrose Street, Glasgow, G1 1XJ, UK. Contact e-mail: paranjayee.mandal@strath.ac.uk

Manuscript submitted August 8, 2019.  
Article published online March 29, 2020

enhanced machinability. For a coarse-grained starting microstructure, the grain refinement can be achieved by cyclic heat treatment, where  $\alpha \rightarrow \gamma \rightarrow \alpha$  phase transitions occur during heating and cooling. Typically, a fine-grain homogeneous microstructure provides a combination of high strength and fracture toughness as per the Hall–Petch relationship, thus it is preferred over a coarse-grained microstructure.<sup>[5]</sup>

Normalizing, carburizing, hardening, and tempering are the recommended heat treatments in order to impart the desired microstructure and mechanical properties in the case-hardened 18CrNiMo7-6 steel.<sup>[1,6,7]</sup> Both carburizing and tempering improve case toughness without significantly affecting the hardness value of the base metal. In addition to this, tempering reduces the possibility of the grinding cracks, which have detrimental effect on the mechanical properties of the material.<sup>[1]</sup> Annealing is useful to eliminate the banded microstructure, whereas the sub-zero treatment at  $-80\text{ }^{\circ}\text{C}$  allows reduction of retained austenite by martensitic transformation eventually leading to higher hardness but lower wear resistance and impact strength of the material.<sup>[8]</sup> In a previous study, the effects of these heat treatment steps on the microstructure of hot forged case-hardened 18CrNiMo7-6 steel were discussed and it was observed that a particular combination of these heat treatment steps led to a very refined microstructure with a prior austenite grain size (PAGS) almost half the size of that as achieved by other combinations.<sup>[9]</sup> A variation in PAGS may result in the same martensitic microstructure after heat treatment, but can influence fatigue resistance, impact strength, yield strength, and hardness in different ways.<sup>[10]</sup> A microstructure with smaller PAGS is always desired considering material toughness.<sup>[11]</sup>

Machining from standard wrought bar stock followed by a multi-step heat treatment is a popular manufacturing route for various machine drive components. The machined components provide an effective and affordable solution when they are used in less demanding environments. If the application demands higher strength, toughness, and durability of the components, then forging is the most suitable option. In general, forging not only increases the strength and toughness of the material, but also refines the grain structure and grain flow, improves part integrity and significantly reduces the material waste. Depending on the forging temperature, it can be classified as cold (at room temperature), warm (above the cold forging temperature range but below the recrystallization temperature of the material), or hot (temperature higher than the recrystallization temperature). Cold forging is advantageous in terms of providing higher strength and hardness because of strain hardening, directional grain orientation, precise geometrical tolerances, better surface finish, reduced tool wear, faster production rate, and reduced energy consumption. However, the main disadvantage of this process is the material fracture due to loss of ductility, which indicates that the particular material must be hot forged. In contrast, the ductility of the material is hugely improved when heated over recrystallization temperature during hot forging. This not only allows a substantial shape change but also improves

grain flow and eliminates porosity of the material. Yet, the hot forging has certain disadvantages over cold forging such as poor geometrical tolerances, poorer surface finish, increased tool wear, significant amount of scale and oxides formation, lower productivity, and higher energy consumption.<sup>[12]</sup> Both hot and cold forging have their individual advantages and disadvantages for applications in demanding environments. Here, it should be noted that the forging processes are not typically considered among the eco-friendly manufacturing processes; however, cold forging is probably the most eco-friendly process of its kind in operation now-a-days. In order to reduce the carbon emission during manufacturing, the cold forging is notable because of its capability in waste reduction due to efficient utilization of the material and use of less energy compared to alternative forging operations that use heat. It has been reported that the cold forging is one of the most cost-effective production processes in today's market because of a high manufacturing speed of up to 450 parts/min<sup>[13]</sup> and  $\sim 40$  to 60 pct estimated cost reduction per manufactured part when compared to alternative forging operations.<sup>[14]</sup> When compared to machining, the cold forging operation provides significantly high material saving and product strength. It has been reported that in order to manufacture a horizontal header part from a billet, the machining operation requires a billet volume three times higher than the final component volume, whereas the cold forging operation required the same volume as of the final component. The machined part is more susceptible to fatigue and stress corrosion as the machine cuts are not always optimally aligned with the grain flow, whereas cold rotary forging results in more oriented grain flow with the overall part shape.<sup>[15]</sup>

The open die press forging is the oldest and most common hot forging process. It requires precise control of friction and heat transfer between the workpiece and dies in order to avoid the barrelling effect. Also, post-forging machining is required to achieve the desired shape and dimension. Rotary or orbital forging has become a substitute for this conventional press forging especially in the case of producing thin discs and large flanges that have a high diameter-to-thickness ratio. Currently, the rotary forge applications are limited to the production of only symmetrical parts, although asymmetrical parts can be manufactured *via* rotary forging route. The advantages of rotary forging include a high level of accuracy in single operation, precise geometrical tolerances, better surface finish, reduced tool wear, faster production rate, and reduced energy consumption.<sup>[16]</sup> Thus, the rotary forging may be suitable for production of machine drive components that have a high diameter-to-thickness ratio and operate in challenging environments.

Any material with adequate ductility can be rotary forged, therefore carbon and alloy steels, stainless steels, brass, and aluminum alloys are considered as potential candidates for cold rotary forging.<sup>[16]</sup> Machining of case-hardenable 18CrNiMo7-6 steel followed by multi-step heat treatment is a well-established manufacturing route for different machine drive components. In the

current work, a feasibility study of two alternative manufacturing routes, *i.e.*, (i) hot forging (better grain flow and more homogeneous properties) and (ii) cold rotary forging (better material utilization), has been conducted to determine any microstructural and mechanical property benefits over the conventional route. Moreover, an optimized 6-step heat treatment, as identified in the previous study by the same group,<sup>[9]</sup> was applied to the 18CrNiMo7-6 steel components manufactured using aforementioned three different routes. The microstructure and mechanical property analysis was carried out prior to and after the heat treatment in order to investigate the effect of the optimized heat treatment. It should be noted that the optimized heat treatment used in this work is different (*i.e.*, has reduced number of steps) than AGMA 926 (Recommended Practice for Carburized Aerospace Gearing, revision C99), which includes an 8-step heat treatment for carburized AISI 9310 aerospace gears.<sup>[17]</sup> The microstructural evolution was studied from initial (*i.e.*, as-manufactured component without any heat treatment) to final (*i.e.*, after completion of the heat treatment on the as-manufactured component) process steps with a particular focus on the intermediate heat treatment step, *i.e.*, hardening. Optical microscopy and electron backscatter diffraction (EBSD) were used to study the microstructure and texture evolution of the components, whereas hardness, electro-thermal mechanical testing (ETMT), and rotary bending fatigue testing (RBFT) were carried out to determine changes in the mechanical properties. The *originality* of this work lies in demonstrating the impact of the optimized 6-step heat

treatment on the alternative manufacturing routes in order to determine whether it produces equivalent or better properties in the final flat cylindrical-shaped machine drive components over the conventional manufacturing route.

## II. EXPERIMENTAL DETAILS

### A. Hot Forging and Cold Rotary Forging Operations

The chemical composition of the 18CrNiMo7-6 steel is shown in Table I. The material was received as a cylindrical-shaped preform in the spheroidized annealed condition. A flat cylindrical-shaped component made by the current manufacturing route, *i.e.*, machining, was supplied as the reference. For the hot forging manufacturing route, the preforms were forged to flat cylindrical-shaped components at 1100 °C using AFRC's in-house Schuler screw press. Similarly, for the cold rotary forging operation, the preforms were forged into a bottom die cavity in order to create a complex component profile using AFRC's 200T MJC rotary forge machine. The photographs of the preforms and the respective final forged components are shown in Figure 1. It should be noted that the preforms used in both alternative routes and therefore the final manufactured components manufactured by those routes have different geometries. However, they are chosen in such a way that despite having different geometries, the final components always show same increment in the diameter and reduction in the thickness and therefore

Table I. Chemical Composition of the 18CrNiMo7-6 Steel (used in this work)

Element	C	Si	Mn	Cr	Ni	Mo	Fe
Wt Pct	0.17	0.27	0.51	1.65	1.53	0.27	balance
Element	P	S	Ti	Al	N	Nb	
Wt Pct	0.01	0.024	< 0.002	0.023	0.009	< 0.003	

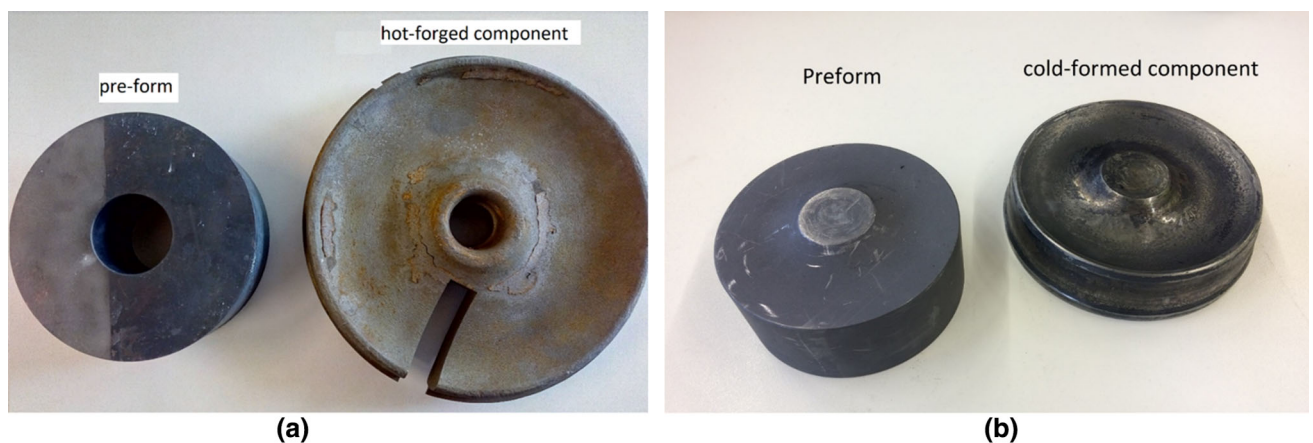


Fig. 1—(a) Preform and hot forged component and (b) preform and cold rotary forged component made by 18CrNiMo7-6 steel (no scale bar is given due to IP restriction).

comparable strains with respect to the preforms. This makes them comparable with each other from material-property related point of view.

### B. Heat Treatment and Sample Extraction from the 18CrNiMo7-6 Steel Components

Table II summarizes the details of the complex multi-step heat treatment as applied on the as-machined, hot forged, and cold rotary forged 18CrNiMo7-6 steel components. The multi-step heat treatment includes six steps—(i) normalizing at 875 °C for 30 minutes followed by air cooling (AC), (ii) carburizing at 930 °C until a 2.6-mm-thick carburized layer is formed, followed by cooling to 820 °C and hold for 1 hour followed by oil quenching (OQ), (iii) annealing at 670 °C for 2 hours followed by AC, (iv) hardening at 800°C for 30 minutes followed by OQ, (v) sub-zero treatment at – 80°C for 90 minutes, (vi) tempering at 200°C for 2 hours followed by AC. Among these six steps, only the carburizing step followed by OQ improves mainly surface hardness with negligible effect on the core properties, whereas the other five steps are intended to improve the properties of the ductile core. Thus, the carburization step was intentionally left during the experimentation of this work and therefore is excluded from Table II. The as-manufactured components experiencing no heat treatment are considered as references for the respective manufacturing routes, denoted by Step0 in Table II.

Six block specimens were extracted using EDM from the periphery of the as-machined component and these extracted block specimens were numbered as S1 to S6. S1 did not undergo any heat treatment (NO heat treatment, referred as Step0 in Table II), whereas the other five blocks were placed together in the furnace and then each block was removed after completion of each of the five process steps. Thus, S2 to S6 represent five steps of heat treatment on the as-machined component as mentioned in Table II. Similarly, six block specimens from the hot forged (S7 to S12) and the cold rotary forged (S13 to S18) components were extracted and given the same heat treatment as previously described for the as-machined component. Thus, properties of machining, hot forging and cold rotary forging manufacturing routes after heat treatment are represented by samples S6, S12, and S18, respectively.

### C. Sample Preparation and Measurement of Microstructural Properties: Optical, EBSD, and Hardness

After the heat treatment operation, all these blocks were cut longitudinally using a Buehler IsoMet 5000 and mounted in conductive resin molds for metallurgical preparation. The mounted samples were ground with SiC abrasive grit papers of different sizes (P240, P400, P800, and P1200) and polished using a UltraPol 9 μm, Trident 3 μm, MasterTex 1 μm, and Microcloth with 0.02 μm colloidal silica suspension in a Buehler EcoMet 300 machine. All samples were etched using Nital (solution of 2 pct HNO<sub>3</sub> in ethanol) to reveal the general microstructure and a Leica DM1200M was used to capture the

**Table II. Multi-step Heat Treatment Applied on the As-machined, Hot Forged, and Cold Rotary Forged Components**

Process Step No.	Process Step Name	Details of the Process Step	Sample Numbers					
			Heat Applied	Treatment Steps	As-machined	Hot Forged	Cold Rotary Forged	
Step0	—	as-manufactured components experiencing NO heat treatment	NO		S1	S7	S13	
Step1	Normalizing	normalizing at 875 °C for 30 minutes + AC	1		S2	S8	S14	
Step2	Annealing	annealing at 670 °C for 2 hours + AC	1 + 2		S3	S9	S15	
Step3	Hardening	hardening at 800 °C for 30 minutes + OQ	1 + 2 + 3		S4	S10	S16	
Step4	Sub-zero quenching	sub-zero treatment at – 80 °C for 90 minutes	1 + 2 + 3 + 4		S5	S11	S17	
Step5	Tempering	tempering at 200 °C for 2 hours + AC	1 + 2 + 3 + 4 + 5		S6	S12	S18	

optical micrographs maintaining ASTM standard E112-13.<sup>[18]</sup> Then, few of the selected samples (Step0, Step3, and Step5 from all three routes) were repolished followed by overnight vibro-polishing with colloidal silica using a Buehler Vibromet vibratory polisher for EBSD analysis. The EBSD data were collected using a FEI Quanta FEG 250—SEM fitted with an Oxford Instruments camera system and Aztec software operating with an accelerating voltage and working distance of 20 kV and 20 mm, respectively. Orientation mapping was performed on a rectangular grid with a step size of 0.5  $\mu\text{m}$ . The indexing was  $\sim 98$  pct for all samples except  $\sim 83$  pct for S18. The heat-treated samples (Step3 and Step5) exhibited the martensitic microstructure consisting of packets, blocks, and laths. Historically, the packet size was termed as the effective grain size in lath martensitic steels due to Hall–Petch relationship observed between the yield strength and the packet size for Fe-Mn alloy.<sup>[19]</sup> The Hall–Petch relationship was also reported between the yield strength and packet size for Fe-0.2C alloy, whereas the yield strength was related to true block width for Fe-0.2C-2Mn alloy. Thus, the blocks were also considered as the effective grains beside packets.<sup>[20]</sup> Typically, the strength and toughness of the lath martensitic steels are strongly dependant on both the packet and block sizes<sup>[21]</sup> and therefore together they are often termed as effective grain size.<sup>[22]</sup> The same terminology has been used in this work. The packets and blocks within the PAGS are often identified by high-angle grain boundaries (HAGB) with a misorientation angle of  $\theta > 15$  deg rather than PAGS and this identification is accepted when the minimum size of accepted grain is consisted of 4 pixels.<sup>[23]</sup> In this work, the minimum size of accepted grains was taken as 5 pixels as per F. J. Humphreys work.<sup>[24]</sup> This indicated that the minimum grain area should be 2.5  $\mu\text{m}^2$  in this case as the step size was 0.5  $\mu\text{m}$ . Anything smaller than this area was considered as noise and therefore was not included in the average effective grain size calculation to avoid underestimation. The EBSD data processing was then carried out using HKL Channel5 post-processing software. The processed data were used to plot the kernel average misorientation (KAM) map. The average misorientation between each individual point and its fourth nearest neighbor kernels was calculated within a rectangular grid ( $9 \times 9$ ) with a 2-deg threshold angle for sub-grains. Since the finite element simulation of the formed components was not within scope of the project associated with the current work, the KAM maps are used to understand the strain distribution of all three as-manufactured components (step0) and at different heat treatment steps (Step3 and Step5).

A Struers hardness tester was used for hardness measurement of all samples according to ASTM standard E384-11.<sup>[25]</sup> The indents were made in a rectangular matrix with a minimum of 100 indents along the sample cross-section using a Vickers indenter with a fixed load of 1 kgf. The distance between any two indents along both  $X$  and  $Y$  directions was kept as 1 mm, which ensured more than 3 diagonal widths spacing between any two indents as typically recommended for steel samples.<sup>[26]</sup>

#### D. Measurement of Mechanical Properties: ETMT and RBFT

The tensile tests were conducted using Instron electro-thermal mechanical testing (ETMT) equipment in conjunction with digital image correlation (DIC) technique and the related experimental setup is shown in Figure 2. The tensile specimens were extracted in the same direction (*i.e.*, perpendicular to the forging axis) from all as-manufactured components (Step0) and after the heat treatment (Step5). Figure 3 shows the geometry of one such ETMT specimen. All test specimens were sprayed with white paint followed by black paint to create a speckle pattern prior to the testing and then subjected to a 50 N preload. The tests were then carried out at room temperature and at a strain rate of 0.001  $\text{s}^{-1}$ . The DIC DaVis<sup>TM</sup> digital image correlation software was used to monitor strain evolution in the gauge length. The ETMT tests were performed following the NPL Good Practise guide for miniature ETMT results.<sup>[27]</sup> Each test was repeated three times for a particular material condition (such as Step0 or Step5) in order to have a good statistical representation of the tensile properties and the values were averaged to obtain the average yield strength (YS) and ultimate tensile strength (UTS). The YS was calculated at a strain offset of 0.2 pct and the UTS was determined from the maximum stress value reached from each of the tests.

The rotary bending fatigue testing (RBFT) was used to measure the fatigue properties of the as-manufactured components before and after heat treatment maintaining ISO 1143:2010 standard.<sup>[28]</sup> The fatigue samples, having 4 mm diameter  $\times$  57 mm length, were extracted from the as-manufactured components (Step0) and after the heat treatment (Step5) perpendicular to the forging direction. The rotating velocity was fixed at 3000 RPM and the fatigue tests were initiated at ambient temperature with applied load of 1000 MPa until the specimen rupture. This load was then gradually reduced for the rest of the specimens till the fatigue limit was obtained. The fatigue limit was defined as the maximum stress for fatigue life of  $10^7$  cycles and subsequent data were compiled into stress–life (S–N) curves.

### III. RESULTS

#### A. Effect of Heat Treatment on Microstructural Properties

Figure 4 shows the optical micrographs indicating the effect of individual heat treatment steps on as-machined microstructure (Step0 to Step5, samples S1 to S6, Table II). The as-machined sample (Step0, S1) had a mixture of a typical pearlitic and ferritic microstructure. Normalization (Step1) was done at a temperature higher than the austenite transformation ( $A_{c3}$ ) and the air cooling (AC) produced a mixture of bainitic and ferritic microstructure. In the next step, annealing followed by AC (Step2) reduced the hardness of the material and relieved the internal stresses. The high temperature during hardening (Step3) produced a larger amount of austenite, but the oil quenching (OQ) ultimately led to

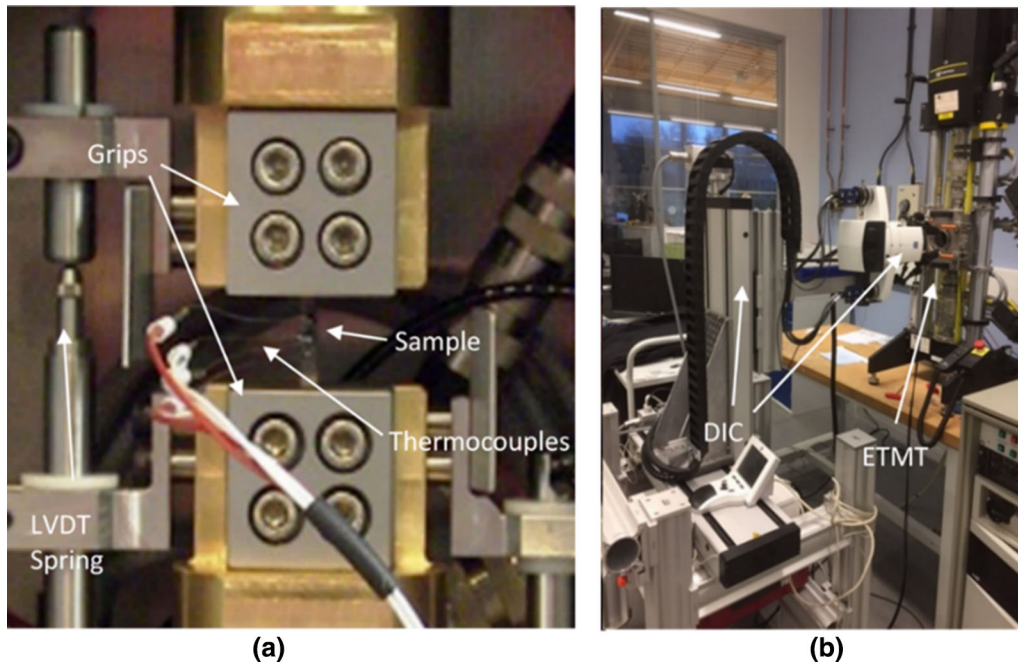


Fig. 2—Images showing the (a) ETMT and (b) DIC experimental setup.

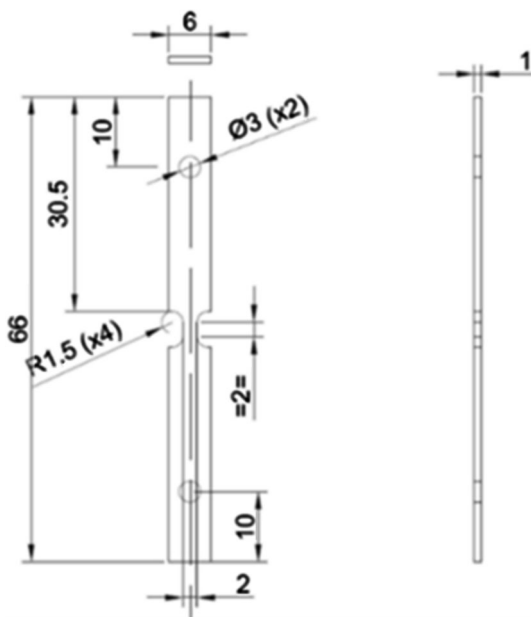


Fig. 3—Geometry of an ETMT specimen (all dimensions are in mm).

the formation of acicular martensitic laths. This was further accelerated during sub-zero treatment (Step4), which produced a finer needle-like martensitic structure. The tempering (Step5) provided acceptable toughness by lowering the hardness and maintained the martensitic microstructure.

Figure 5 shows the optical micrographs indicating the effect of individual heat treatment steps on hot forged microstructure (Step0 to Step5, samples S7 to S12, Table II). The hot forged sample (Step0, S7) had a

mixture of a bainitic-ferritic microstructure and the large prior austenite grains were also clearly visible. This microstructure was retained after both normalization and annealing steps. The hardening step followed by OQ produced acicular martensitic laths, which was further accelerated during the sub-zero treatment leading to finer needle-like martensitic structure. This microstructure was maintained until tempering step. Similarly, Figure 6 shows the optical micrographs indicating the effect of individual heat treatment steps on cold rotary forged microstructure (Step0 to Step5, samples S13 to S18, Table II). The cold rotary forged sample (Step0, S13) showed a mixture of pearlitic-ferritic microstructure similar to the as-machined sample (Step0, Figure 4). Both the normalization and the annealing steps produced a bainitic-ferritic microstructure and it was possible to observe the prior austenite grain boundaries from these micrographs (Step1 and Step2 in Figure 6). The hardening step followed by OQ produced acicular martensitic laths, which was further accelerated during the sub-zero treatment leading to a finer needle-like martensitic structure. This was maintained till the end of tempering. Overall, the cold rotary forged sample showed a microstructural evolution very similar to the as-machined sample before and after the heat treatment.

A fine-grain homogeneous microstructure is always preferred over a banded microstructure in order to achieve isotropic mechanical properties. In this work, the banded microstructure was observed in the as-machined sample (Step0, Figure 4) and after cold rotary forging (Step0, Figure 6). But the multi-step heat treatment transformed this banded microstructure into tempered martensitic microstructure irrespective of the above-mentioned process routes (Step5 in both

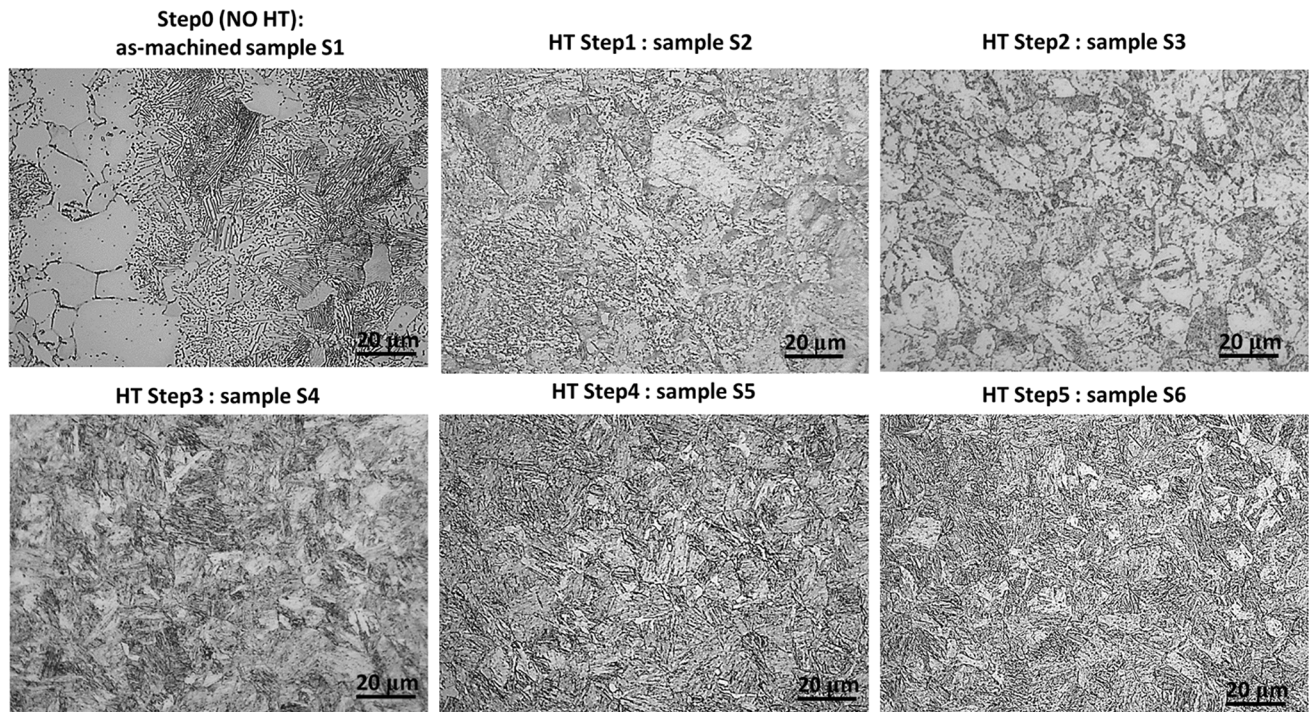


Fig. 4—Optical micrographs showing effect of individual heat treatment steps on as-machined microstructure.

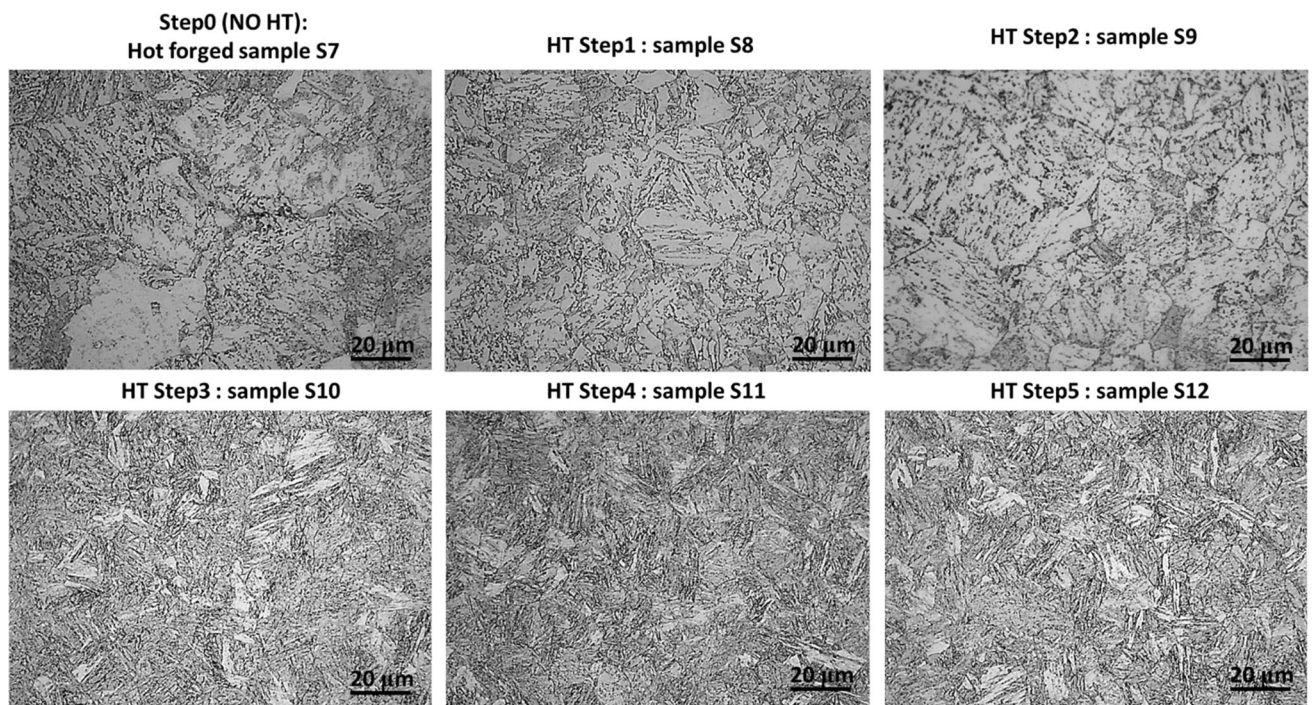


Fig. 5—Optical micrographs showing effect of individual heat treatment steps on hot forged microstructure.

Figures 4 and 6). On the other hand, the hot forging eliminated the banded microstructure (Step0, Figure 5) and then the heat treatment led to formation of similar tempered martensitic microstructure (Step5, Figure 5). Thus, the hot forging route is itself effective in

eliminating the banded microstructure, whereas the multi-step heat treatment is required for both machining and cold rotary forging routes.

Figure 7 shows the effectiveness of the heat treatment on the grain flow and microstructure of the hot forged

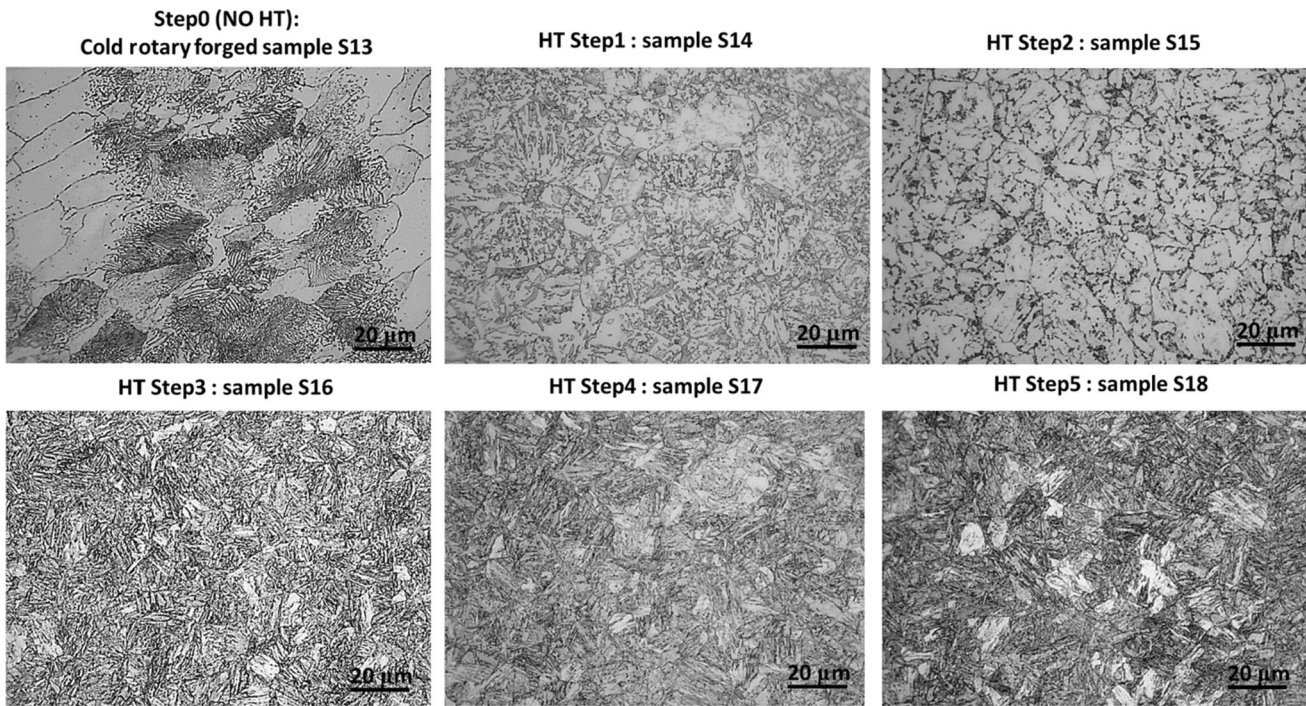


Fig. 6—Optical micrographs showing effect of individual heat treatment steps on cold rotary forged microstructure.

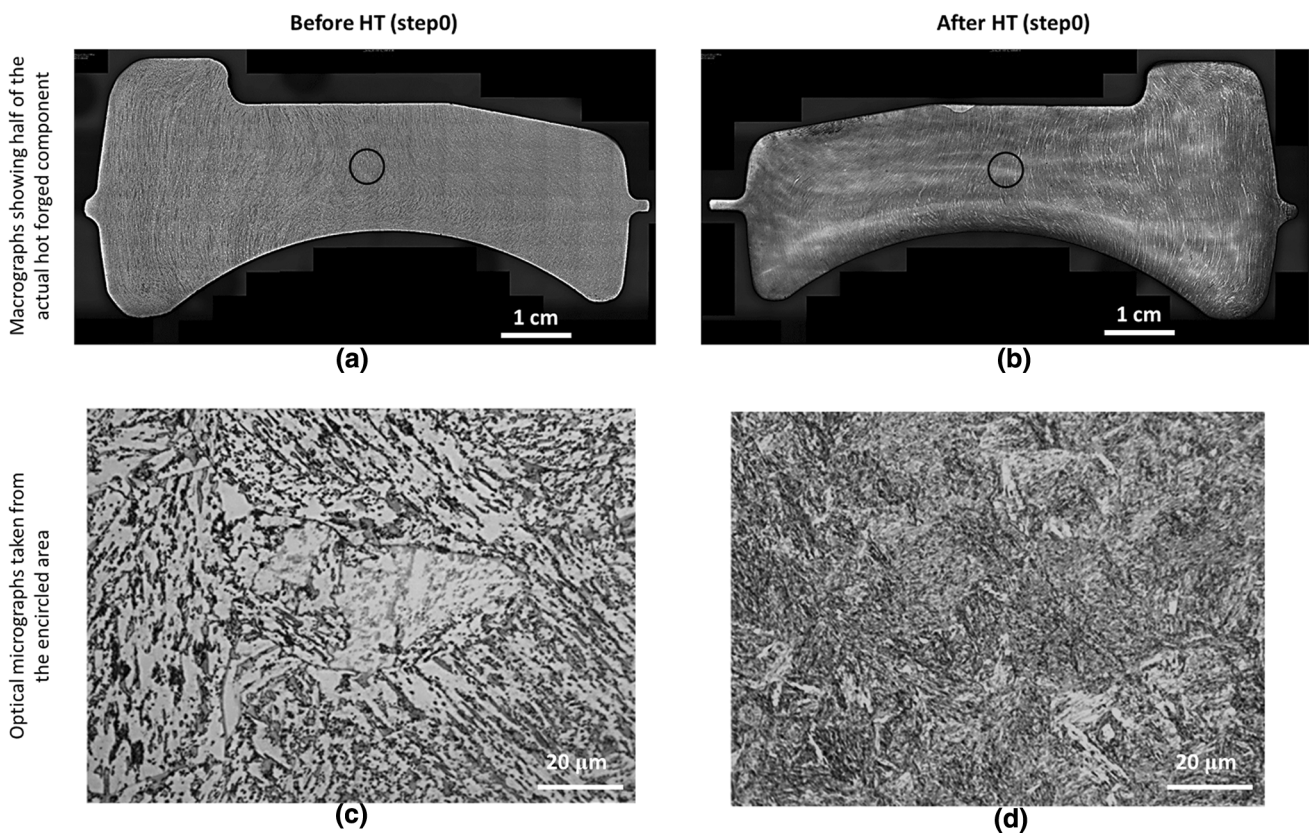


Fig. 7—Effectiveness of the heat treatment on the (a, b) grain flow (scale length 1 cm) and (c, d) microstructure of actual hot forged component.



component. The actual hot forged component has a symmetrical flat cylindrical disc shape, thus the macrographs show only half of the component before and after the heat treatment. The macrograph showing the component before heat treatment indicated material flow towards the outside diameter (Figure 7(a)) and after the heat treatment, no change in the grain flow was observed (Figure 7(b)). The optical micrographs taken from the center of the component (locations of the micrographs are encircled in black) before and after the heat treatment (Figures 7(c) and (d), respectively) showed complete absence of the banded microstructure. Similarly Figure 8 shows the effectiveness of the heat treatment on the grain flow and microstructure of the cold rotary forged component. The macrograph showing half of the symmetrical cold rotary forged component (Step0, Figure 8(a)) indicated a significant difference in the material flow from the top and bottom sides compared to the center, notably a band showing a difference in the grain flow was observed along the transverse direction. The banded microstructure was evident from the optical micrograph (Figure 8(c)). The heat treatment eliminated the banded microstructure (Figure 8(d)) and in turn improved the grain flow (Figure 8(b)).

It is important to note that a pearlitic-ferritic microstructure is obtained *via* both machining and cold rotary forging routes whereas hot forging route leads to

bainitic-ferritic microstructure. However, the heat treatment transforms them to the same final microstructure, *i.e.*, a finer needle-like tempered martensitic microstructure. For all three components, the martensitic microstructure was obtained at Step3 and then it was retained till the end of the heat treatment. Particularly, this heat treatment eliminated the banded microstructure in both the as-machined (Figure 4) and cold rotary forged components (Figure 6) and simultaneously improved the grain flow of the cold rotary forged component (Figure 8).

For better understanding of the effectiveness of this heat treatment on the microstructural evolution during these three manufacturing routes, EBSD analysis was undertaken and the focus was given at three crucial points, *i.e.*, Step0, Step3, and Step5. Figure 9 shows the band contrast images of the as-machined, hot forged, and cold rotary forged samples at Step0, Step3, and Step5. The different starting microstructures (Step0) of all three manufacturing routes were transformed to martensitic microstructure at Step3 and no further change was observed through Step5.

Figure 10 shows the phase maps of the above-mentioned samples, in which BCC and orthorhombic crystal structures are indicated in yellow and red colors, respectively. Any detected phase with less than 1 pct proportion were considered as a noise and therefore was not considered during the analysis. The main phase

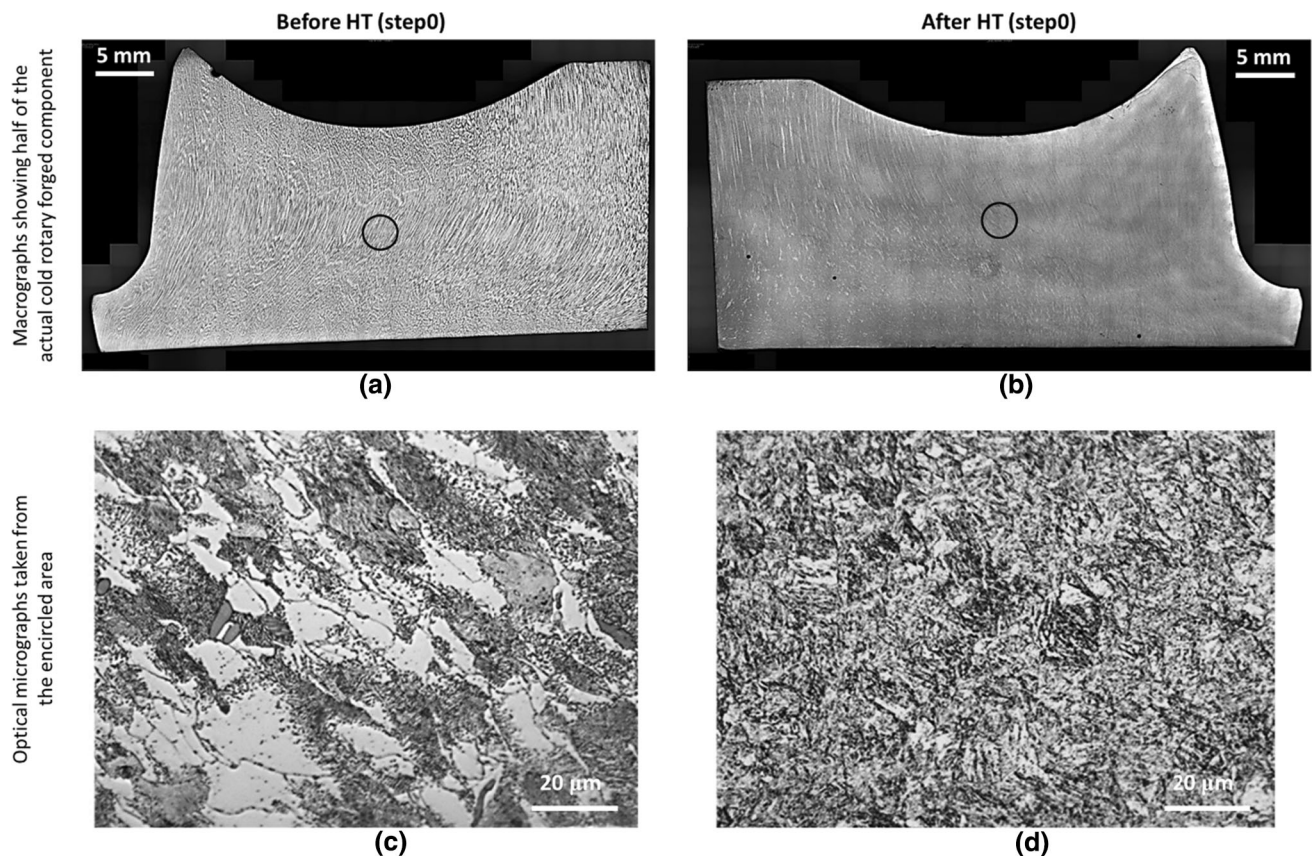


Fig. 8—Effectiveness of the heat treatment on the (a, b) grain flow (scale length 5 mm) and (c, d) microstructure of actual cold rotary forged component.

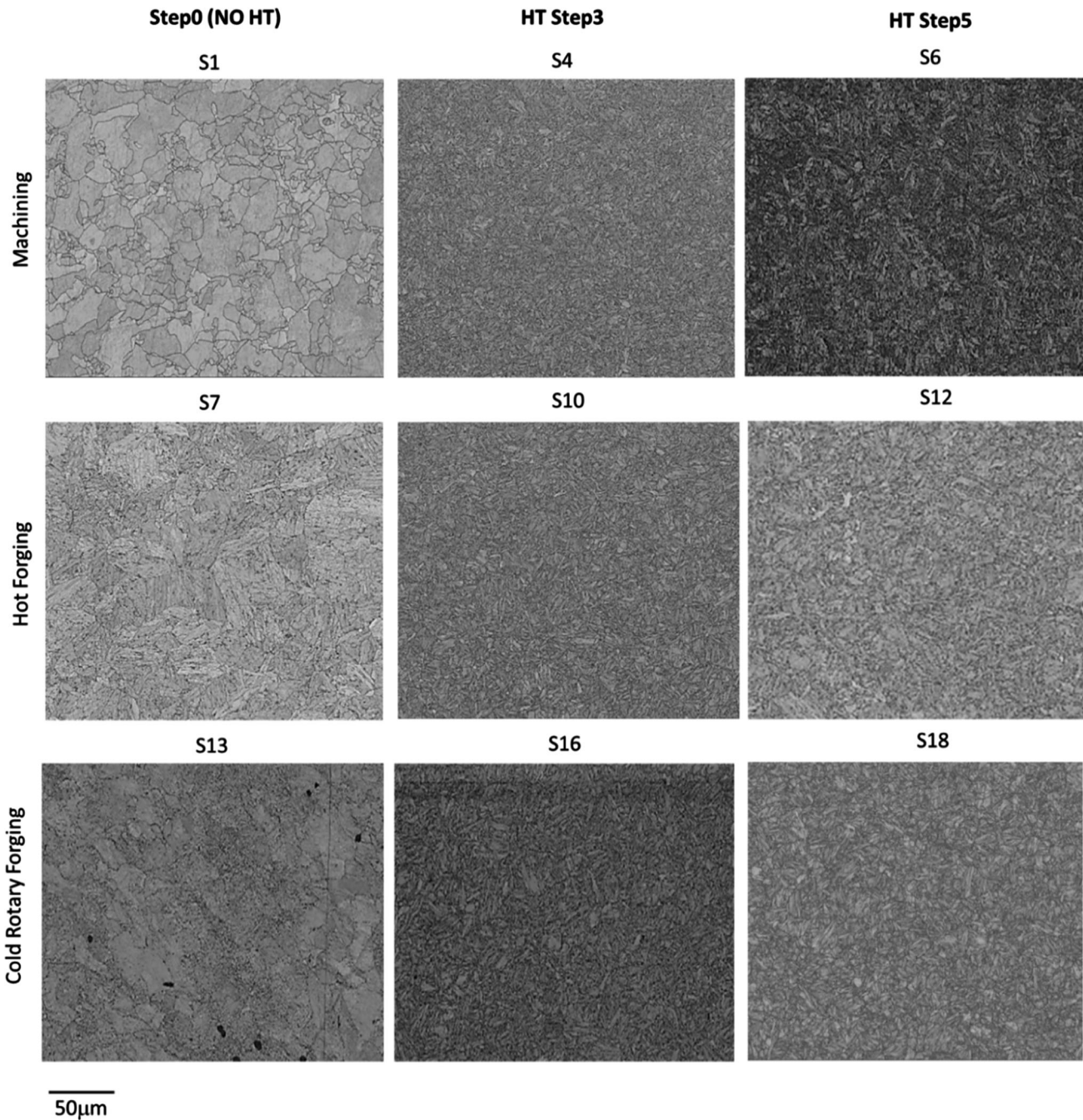


Fig. 9—Band contrast images showing the effect of selected heat treatment steps on different manufacturing routes.

observed in 18CrNiMo7-6 steel was BCC ferrite (97.8 to 99.9 pct) at Step0. At Step3, the BCC martensitic microstructure was formed (98.8 to 99.6 pct). Typically, either BCC or BCT martensitic microstructure was observed in the quenched steel samples depending on the carbon concentration. The microstructure was typically BCC, *i.e.*,  $c/a$  ratio 1, when the carbon concentration was  $< 0.6$  wt pct<sup>[29]</sup> and the same was observed for 18CrNiMo7-6 steel containing  $\sim 0.18$  wt pct carbon. The martensitic microstructure remained as the main phase for both machining (97.8 pct) and hot forging (99.9 pct) routes through Step5, however, a significant difference

was observed for the cold rotary forging route showing the presence of both BCC martensite (75.1 pct) and orthorhombic cementite (7.9 pct) phases. Here it should be noted that the indexing of sample S18 was only  $\sim 83$  pct and therefore there was a fair chance that the unindexed points might belong to either martensite or cementite phases. This noticeable amount of cementite formation observed in S18 needs further investigation. However, it may be influenced due to the lower hardening temperature (800 °C) used in this case than the usual core hardening temperature range (830 °C to 870 °C) for this steel.

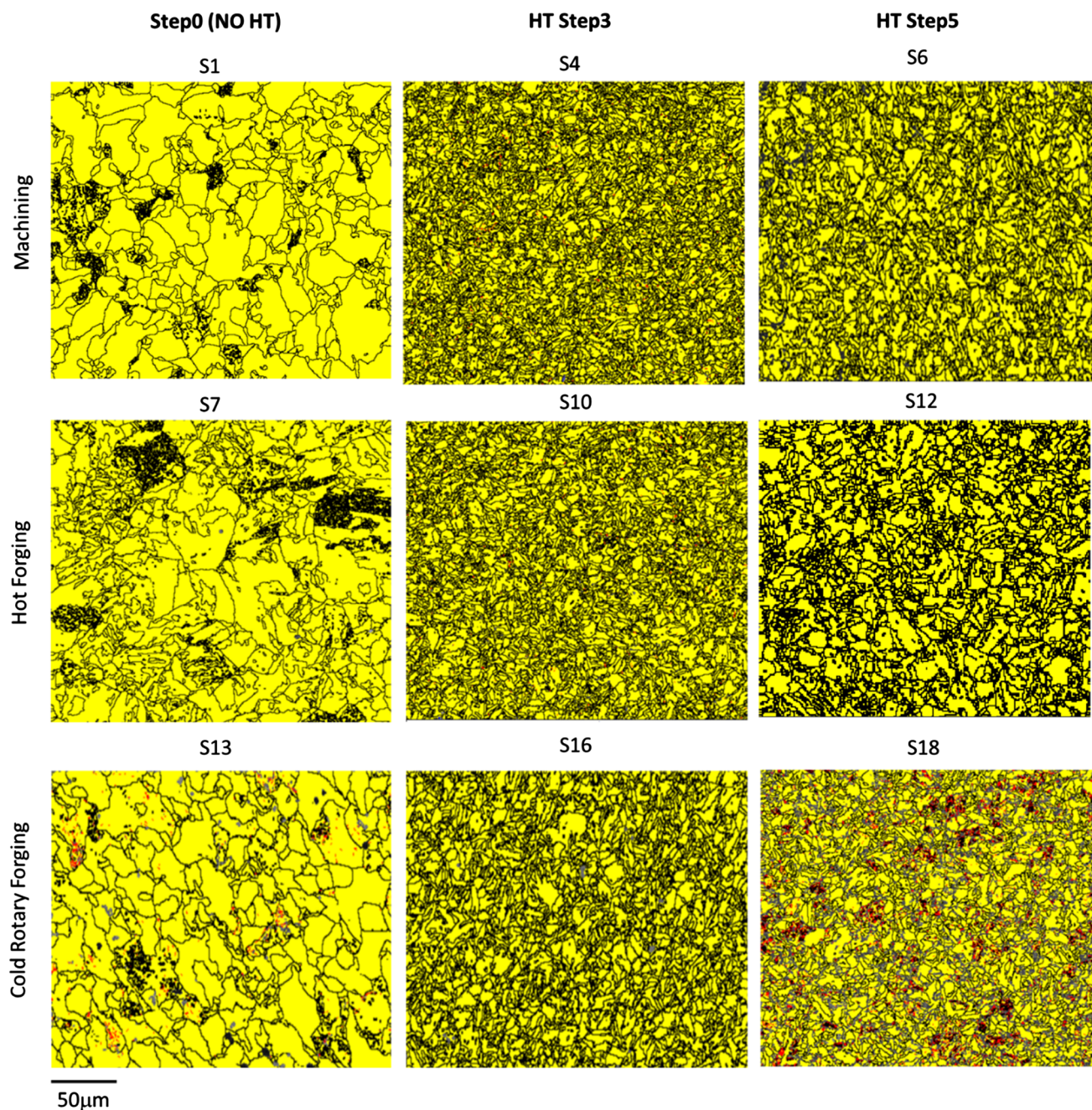


Fig. 10—Phase maps (BCC in yellow, orthorhombic in red) showing the effect of selected heat treatment steps on different manufacturing routes (Color figure online).

Figure 11 shows the effect of selected heat treatment steps on average effective grain size as obtained from the different manufacturing routes. The effective grain size, as identified by a misorientation angle of  $\theta > 15$  deg, was observed largest in the as-machined sample ( $\sim 7.60 \mu\text{m}$  in a pearlitic-ferritic microstructure) and slightly less for both the hot forged ( $\sim 6.40 \mu\text{m}$  in a bainitic-ferritic microstructure) and cold rotary forged ( $\sim 6.31 \mu\text{m}$  in a pearlitic-ferritic microstructure) samples. These different starting microstructures were transformed into acicular martensitic microstructure at Step3, where a significant reduction in the average effective grain size was observed

for all three processing routes ( $\sim 3.04$ ,  $\sim 3.34$ , and  $\sim 3.37 \mu\text{m}$  for machining, hot forging, and cold rotary forging routes, respectively). At Step5, formation of a tempered martensitic microstructure led to a slight increase in the average effective grain size for machining route ( $\sim 3.36 \mu\text{m}$ ), but a slight decrease for both hot forging and cold rotary forging routes ( $\sim 3.1$  and  $\sim 3.06 \mu\text{m}$ , respectively). Figure 12 shows inverse pole figure (IPF) maps in the ND–RD plane indicating random orientation of these grains for all three manufacturing routes. It should be noted that the change in microstructure as well as effective grain size from Step0 to Step3 did not show any

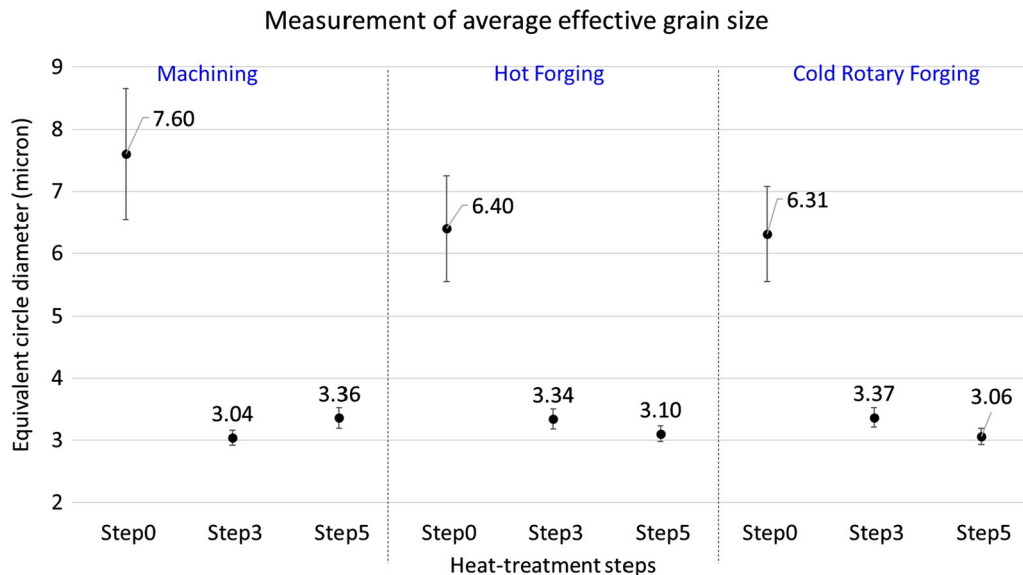


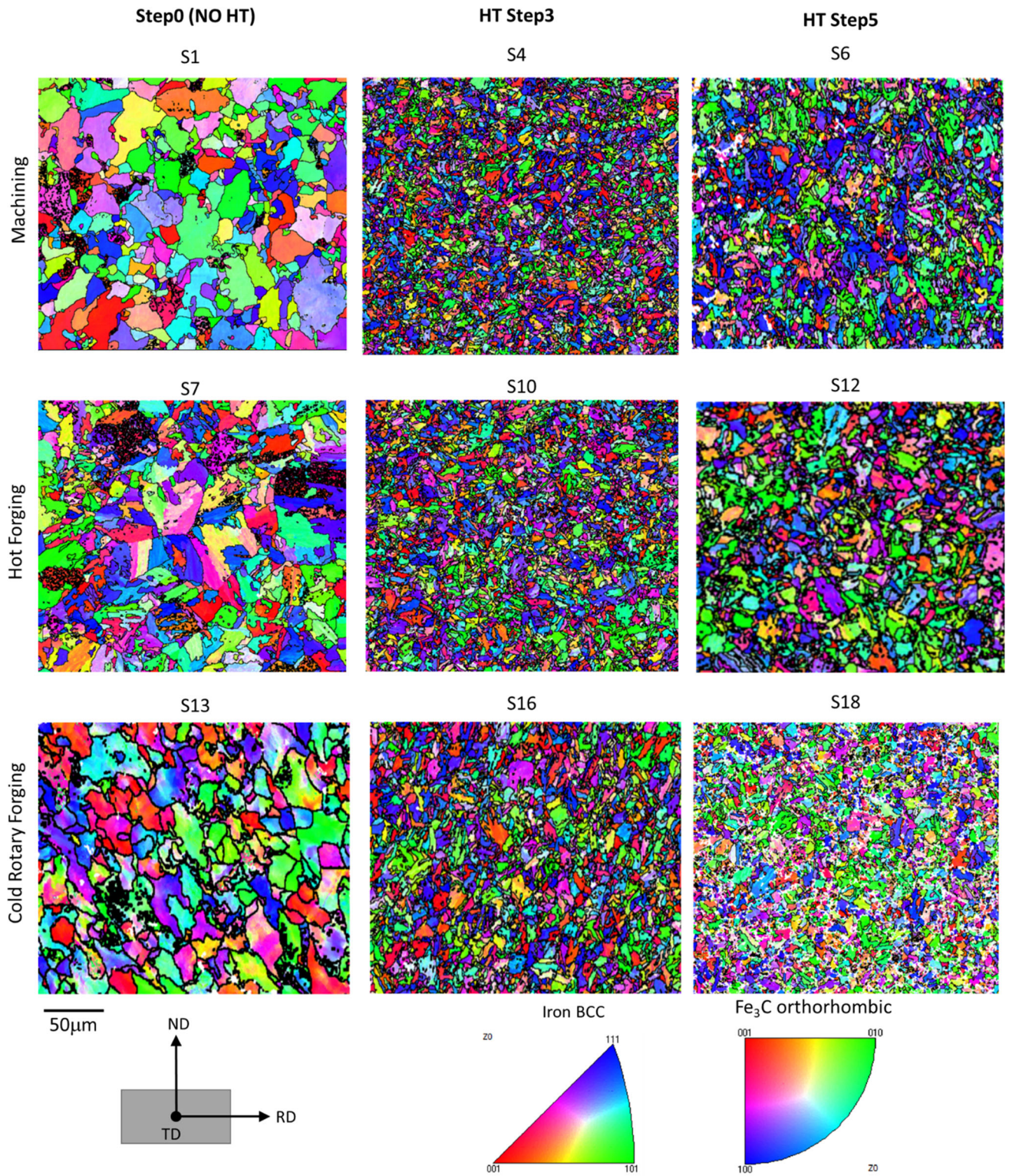
Fig. 11—Effect of selected heat treatment steps on average effective grain size as obtained from different manufacturing routes.

change in the respective grain orientation. Irrespective of the manufacturing routes, this heat treatment resulted in same tempered martensitic microstructure with the average effective grain size in the range of  $\sim 3.06$  to  $3.36 \mu\text{m}$ .

Figure 13 shows the effect of selected heat treatment steps on area fraction of effective grains as obtained from different manufacturing routes. The recrystallized, sub-structured, and deformed grains are shown in blue, yellow, and red colors, respectively, in the area fraction maps and in the summary graph. The deformed grains contain a large number of dislocations and are defined by a misorientation angle  $\leq 5$  deg. The recrystallized grains are the undeformed grains that do not contain stored elastic energy and are defined by a misorientation angle  $\geq 15$  deg. The sub-structured grains are the metastable grains with a fewer number of dislocations and are defined by a misorientation angle ranging from 5 to 15 deg. The initial processing route of the preform led to the formation of a large amount of recrystallized grains ( $\sim 90.5$  pct) in the as-machined sample (Step0). Step3 introduced lattice deformation due to martensitic formation leading to a rise in the dislocation density. This led to an increase in the amount of both sub-structured and deformed grains ( $\sim 49.2$  to  $65.3$  and  $\sim 14.5$  to  $17.2$  pct, respectively), which were maintained through Step5. During hot forging (Step0), the dynamic recrystallization led to formation of a significant amount of recrystallized and sub-structured grains ( $\sim 40.8$  and  $58.3$  pct, respectively). Upon heat treatment (Step3 and Step5), the structural deformation due to OQ led to the formation of a considerable amount of deformed grains ( $\sim 11.5$  to  $14.4$  pct) at the expense of recrystallized and sub-structured grains ( $\sim 34$  to  $35.7$  and  $\sim 51.6$  to  $52.8$  pct, respectively). On the other hand, the cold rotary forged sample (Step0) contained mostly sub-structured grains ( $\sim 88.1$  pct) due to the absence of dynamic recrystallization at low temperature.

Although no dynamic recrystallization occurred at that low temperature, but the energy created by adiabatic heat from the material deformation seemed to be sufficient enough to rearrange the dislocations into lower energy cell structures leading to the formation of mostly sub-structured grains. Upon heat treatment (Step3 and Step5), the sub-structured grains were significantly recrystallized ( $\sim 29$  to  $29.9$  pct) and the deformation due to OQ simultaneously increased the amount of deformed grains ( $\sim 9.07$  to  $13$  pct). In addition to this, the summary graph shows that this heat treatment leads to almost similar area fraction of grains ( $\sim 29$  to  $34$  pct recrystallized,  $51.6$  to  $61.9$  pct sub-structured, and  $9.07$  to  $14.4$  pct deformed grains) for both the hot forging and cold rotary forging routes, but slightly different for the machining route ( $\sim 17.5$  pct recrystallized,  $65.3$  pct sub-structured, and  $17.2$  pct deformed grains).

Figure 14 shows the KAM maps representing the strain distribution at selected heat treatment steps from different manufacturing routes. The plastic strain in the as-manufactured components (Step0) and at different heat treatment steps (Step3 and Step5) are measured using local misorientation approach. The KAM map measures the local misorientations between individual measurement points and thereby represents the strain of the scanned area. The red and blue colors denote the highest and lowest levels of misorientations, respectively, for these scanned areas as shown in the scale bar. As observed, the strain distribution was lowest (denoted by mostly blue and green colors) in the as-machined component, followed by the cold rotary forged and hot forged components, respectively. During heat treatment Step3, the deformation was imparted due to martensitic transformation leading to an increased strain level (denoted by mostly yellow color). At this step, the cold rotary forged component showed lowest strain level. At



ND: Normal direction (forging direction); RD: Radial direction (of the component); TD: Transverse direction

Fig. 12—IPF maps showing orientation of the effective grains at selected heat treatment steps from different manufacturing routes.

Step5, the strain levels were further increased (denoted by mostly yellow and red colors) leading to similar strain distribution despite the differences in the final component geometries for all three manufacturing

routes. These strain levels can be further correlated with the respective average effective grain sizes, where deformation imparted during heat treatment causes substantial grain refinement.

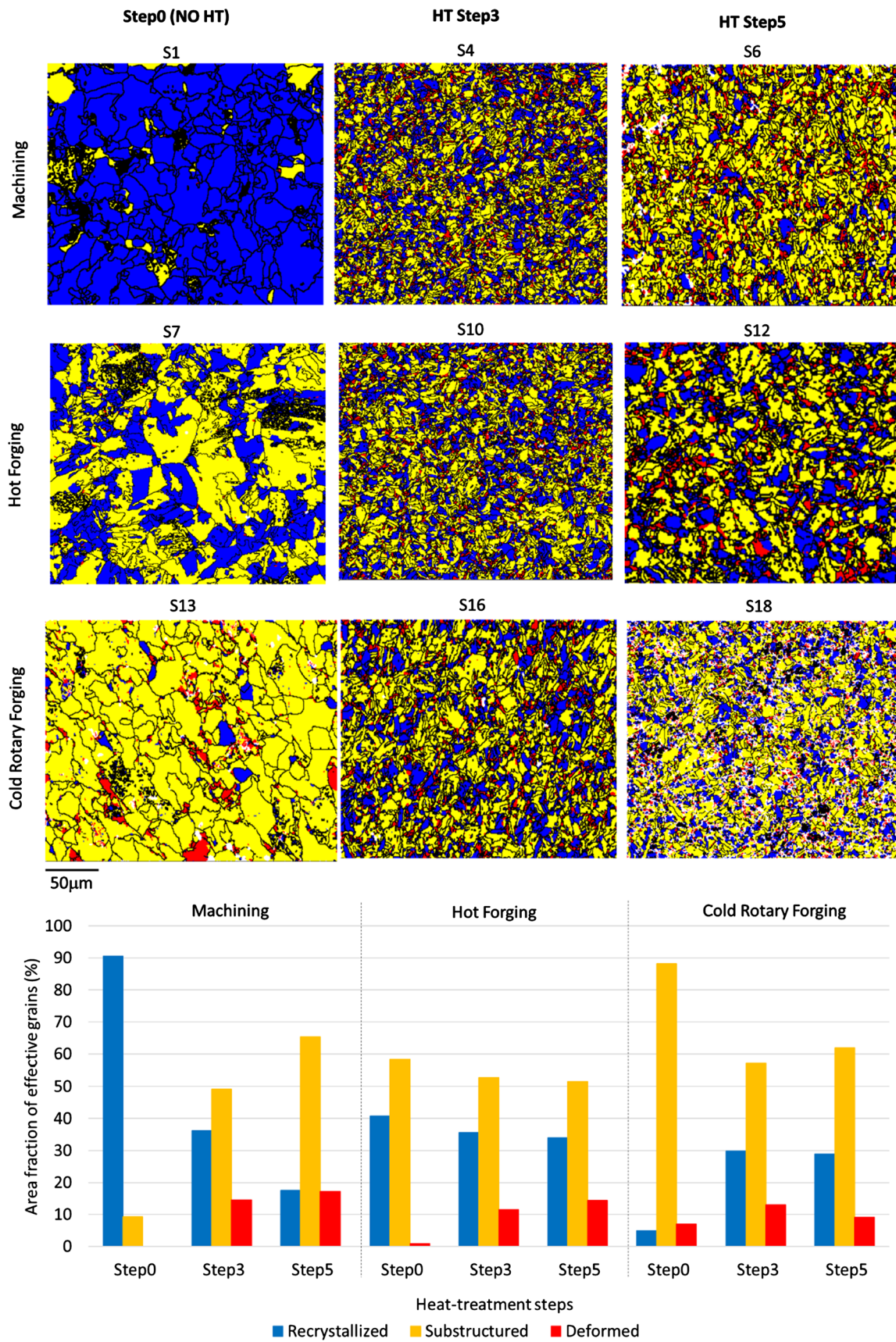


Fig. 13—Effect of selected heat treatment steps on area fraction of effective grains as observed from different manufacturing routes (Color figure online).

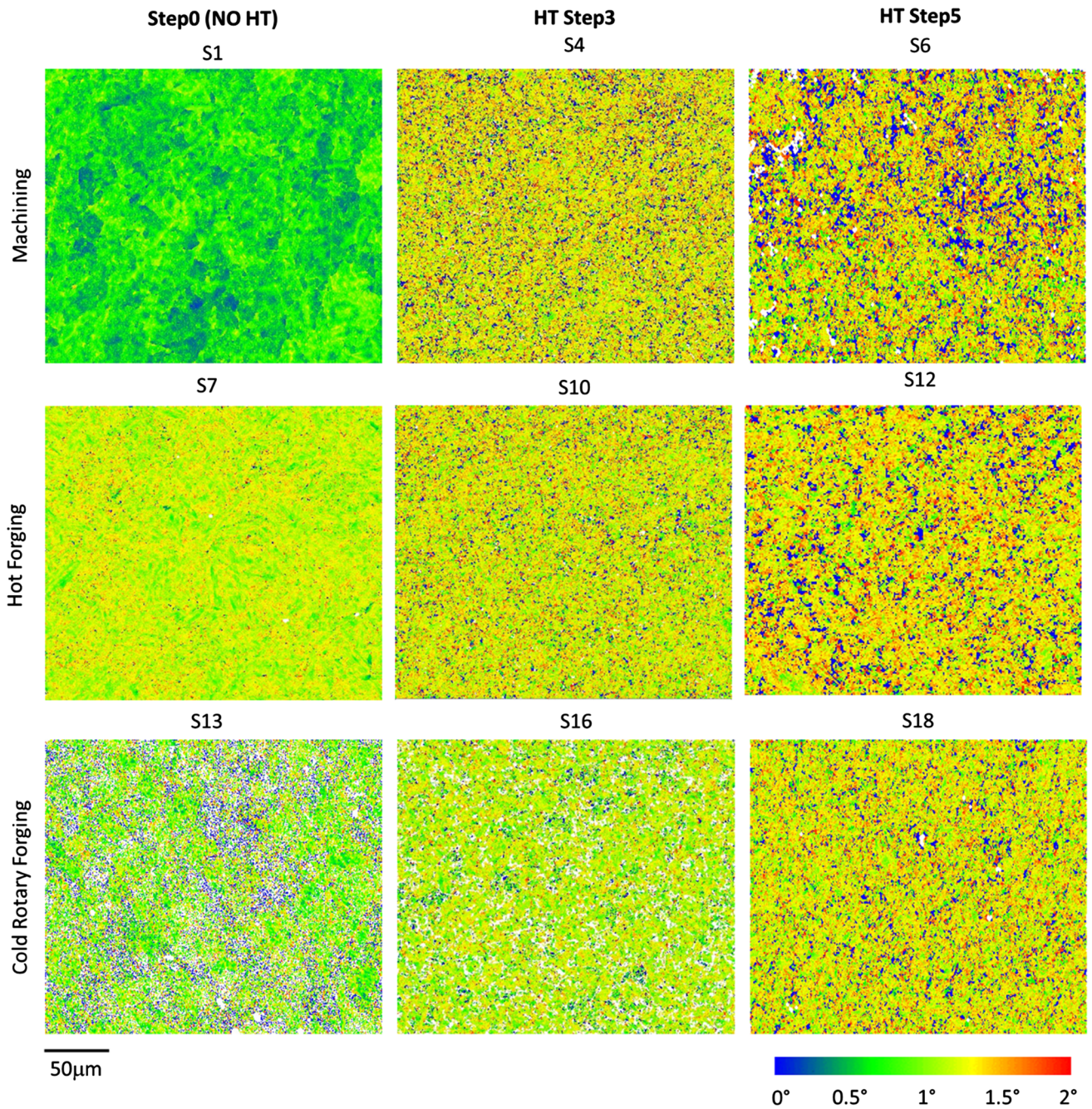


Fig. 14—Kernel Average Misorientation (KAM) maps representing the strain distribution at selected heat treatment steps from different manufacturing routes (Color figure online).

The evolution of crystallographic texture during heat treatment of these three as-manufactured components is noteworthy. The orientation distribution function (ODF) maps are used to represent texture in this work. Typically, the most important ODF section is the  $\phi_2 = 45$  deg section for BCC materials, where  $\Phi$ ,  $\phi_1$ , and  $\phi_2$  are three Euler angles as denoted by Bunge notation.<sup>[30]</sup> The main texture fibers of BCC materials are  $\gamma$ -fibre (111 || ND),  $\alpha$ -fibre (110 || RD),  $\eta$ -fibre (001 || RD),  $\zeta$ -fibre (110 || ND), and  $\varepsilon$ -fibre (110 || TD), and the main texture components are Goss, Brass, Cube, E1, E2, and F1, which are embedded in reduced Euler's space as

observed in two vital ODF sections  $\phi_2 = 0$  deg and  $\phi_2 = 45$  deg.<sup>[31]</sup> In this work, both  $\phi_2 = 0$  deg and  $\phi_2 = 45$  deg sections were plotted for three as-manufactured components (Step0) and during selected heat treatment steps (Step3 and Step5). The contour lines were drawn at a step width of 2 and individual scale bars were plotted below the respective ODF maps showing texture strength for the individual steps.

Figure 15 shows the ODF maps of the as-machined sample and during the heat treatment. Mainly Goss (G) and Brass (B) texture components with a maximum texture strength of 6.54 were observed in the

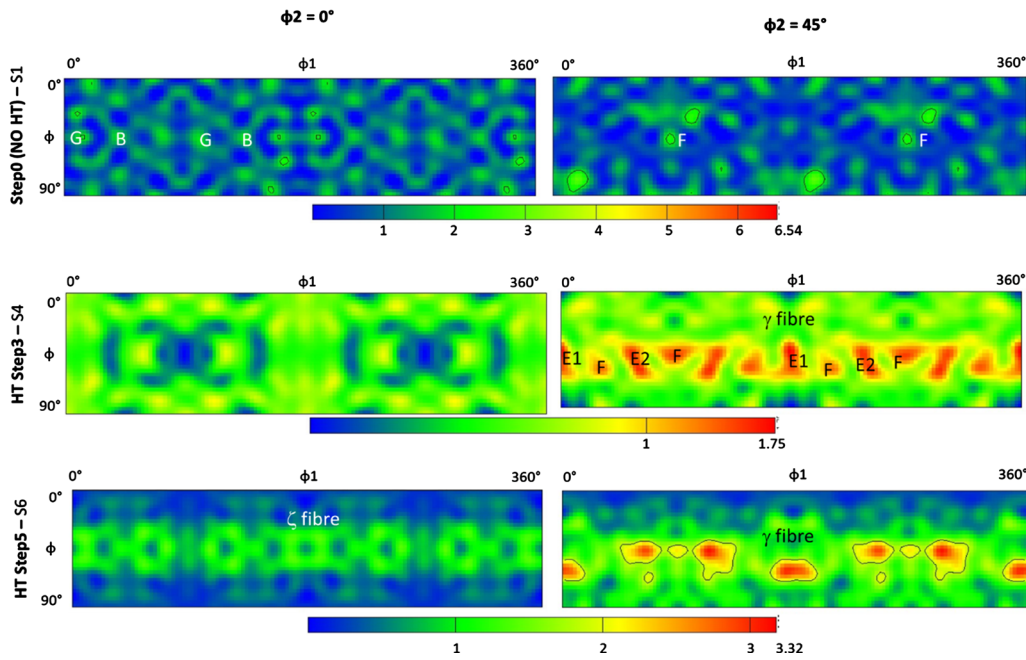


Fig. 15—Effect of selected heat treatment steps on texture evolution of machined steel samples.

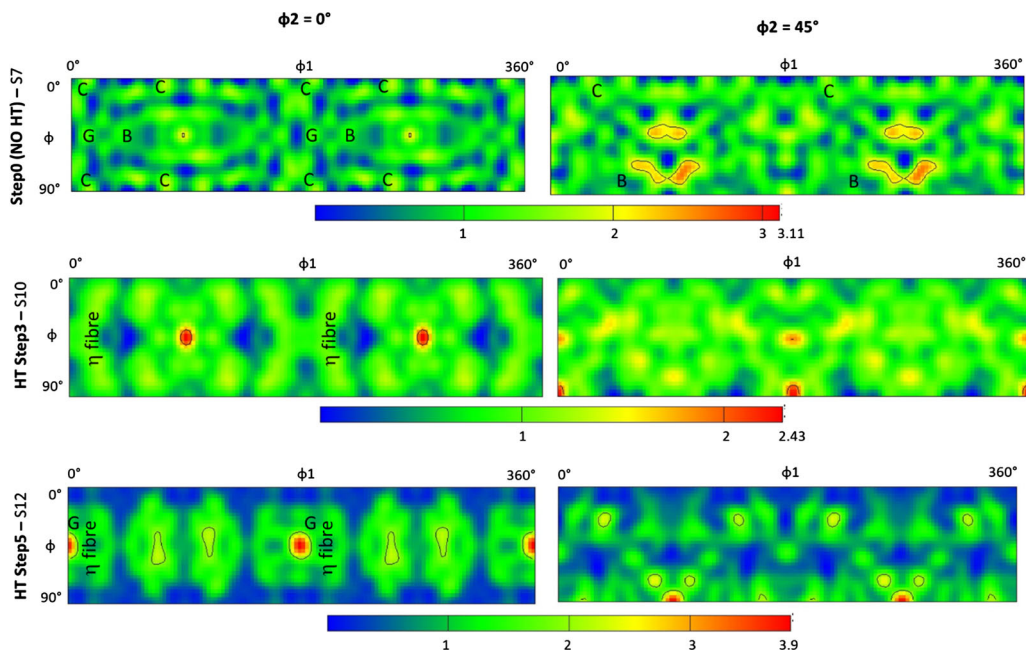


Fig. 16—Effect of selected heat treatment steps on texture evolution of hot forged steel samples.

as-machined sample (Step0). The  $\gamma$ -fibre evolved during Step3 and a significant decrease in the texture strength (1.75) was observed. The presence of  $\gamma$ -fibre along with E1, E2, and F texture components became very prominent at Step5 with a slight increase in the texture strength (3.32). Figure 16 shows the same ODF maps for the hot forged sample. The hot forged sample (Step0) contained mainly the Goss, Brass, and Cube (C) texture components with a maximum texture strength of 3.11. The  $\eta$ -fibre was developed at Step3 but then

disappeared at Step5. No other prominent texture fibers or components were observed at Step5. The texture strength showed no significant change after heat treatment (2.43 and 3.9 for Step3 and Step5, respectively). Figure 17 shows the same ODF maps for the cold rotary forged sample. Mainly Goss and Cube texture components with a maximum texture strength of 9.6 was observed in the cold rotary forged sample (Step0). Upon heat treatment, the Goss and Cube components were retained but no texture fibers were apparently developed



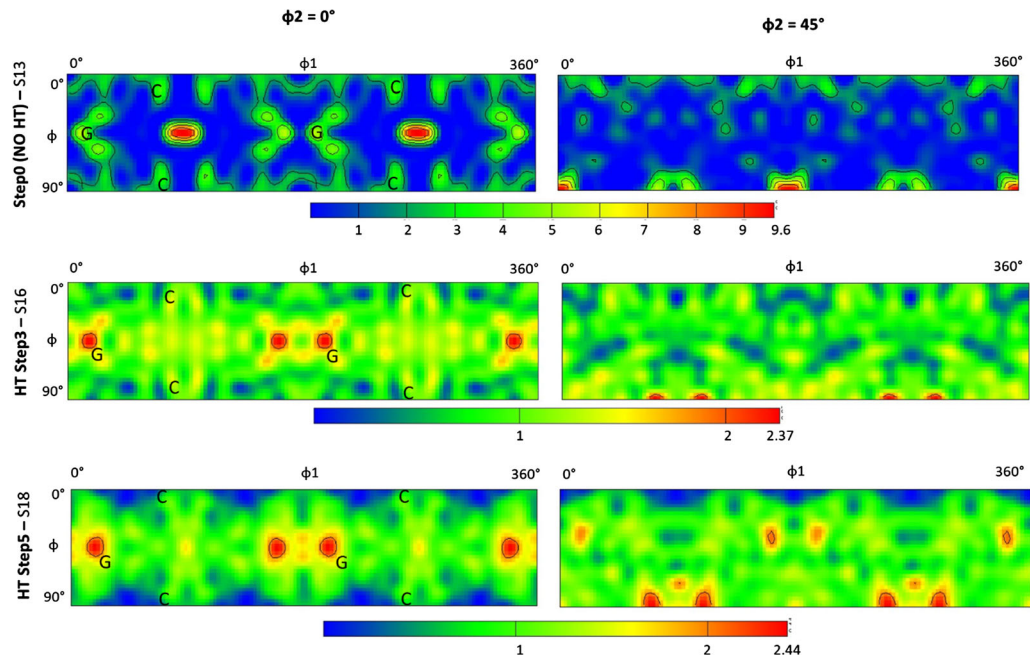


Fig. 17—Effect of selected heat treatment steps on texture evolution of cold rotary forged steel samples.

at Step3 leading to a drastic decrease in the texture strength to 2.37. A hybrid fiber between Brass and Goss texture components was observed at Step5 without changing the texture strength (2.44 at Step5). It is important to note that the  $\gamma$ -fibre is a characteristic texture fiber in rolled BCC material.<sup>[31]</sup> In this study, the  $\gamma$ -fibre was only observed after heat treatment of the as-machined sample (Step5 in Figure 15). The absence of  $\gamma$ -fibre particularly in the hot forged and cold rotary forged samples might be attributed to the deformation imparted during the forging operation followed by the heat treatment.

The BCC texture was visible in all three as-manufactured components, but it was masked during heat treatment because of the martensitic transformation. This was clearly evident from Figures 15 through 17. It was largely recognized that the dynamic recrystallization was responsible for weakening of the texture and the same was observed for the hot forged sample (max texture strength  $\sim$  3.1 MUD). The heat treatment resulted in minor change of the recrystallized fraction of grains in the hot forged sample keeping the weak deformation texture unaffected (max texture strength  $\sim$  3.9 MUD). Likewise, the as-machined sample showed medium texture strength (max texture strength  $\sim$  6.5 MUD), which was again decreased due to recrystallization during heat treatment (max texture strength  $\sim$  3.3 MUD). On the other hand, the cold rotary forged sample showed a very strong deformation texture (max texture strength  $\sim$  9.6 MUD) due to complete absence of dynamic recrystallization. Upon heat treatment, the grains were significantly recrystallized resulting in a significant texture weakening (max texture strength  $\sim$  2.4 MUD). It should be noted here that irrespective of the manufacturing routes, the tempered martensitic

microstructure masked the evolved texture in the heat-treated components resulting in almost similar texture strength (max texture strength  $\sim$  2.4 to 3.9 MUD).

Figure 18 demonstrates the effect of heat treatment steps on average hardness as obtained by all three manufacturing routes. Both as-machined and cold rotary forged samples (Step0) had similar pearlitic-ferritic microstructure, however, the work hardening in cold rotary forged sample led to a smaller effective grain size and therefore higher average hardness of 233 HV as compared to 155 HV hardness of the as-machined sample. The hot forged sample (Step0) having bainitic-ferritic microstructure showed significantly higher hardness of 296 HV. This difference in hardness was minimized during normalization (Step1), where the hot forged sample exhibited slightly reduced average hardness of 284 HV but both the as-machined and cold rotary forged samples showed significant increase in average hardness, 294 and 309 HV, respectively. This is attributed to change in the microstructure from pearlitic-ferritic to bainitic-ferritic. During annealing (Step2), the internal stress was relieved and the average hardness of all three samples was decreased to a range of 219 to 232 HV. After hardening followed by OQ (Step3), the microstructure was transformed to a much harder martensitic phase with a decrease in the effective grain size, which led to subsequent increase in average the hardness to a range of 423 to 450 HV. This high hardness was maintained till the end of heat treatment (415 to 459 HV as observed from Step4 and Step5), although formation of a tempered martensitic microstructure at Step5 slightly decreased the average hardness values. It should be noted that the as-machined, hot forged, and cold rotary forged samples

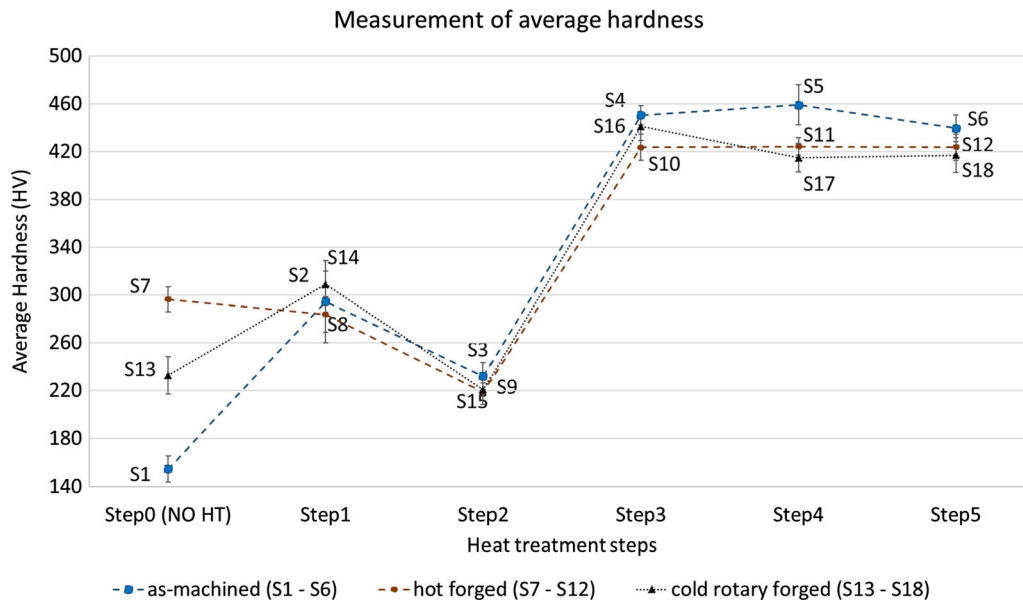


Fig. 18—Effect of heat treatment steps on average hardness as obtained from different manufacturing routes.

showed effective grain sizes of  $\sim 3.36$ ,  $\sim 3.1$ , and  $\sim 3.06$   $\mu\text{m}$ , respectively, and after the heat treatment, their final hardness was observed in the relevant manner (440, 423, and 417 HV, respectively) indicating the applicability of Hall–Petch relationship. A similar behavior was observed by the researchers elsewhere.<sup>[20,21]</sup> It can be concluded that the martensitic transformation and a refined microstructure together improved the hardness of the as-manufactured components after heat treatment.

### B. Effect of Heat Treatment on Mechanical Properties

Figure 19 shows the tensile behavior of as-manufactured components before (Step0) and after (Step5) the heat treatment. The deformation was observed to be identical for all tensile tests per material condition indicating good repeatability of the tensile properties and homogeneity of the material. A notable difference was observed between the stress–strain behavior of both hot forged and cold rotary forged samples. The stress–strain curves showed typical gradual yielding but different YS and UTS values. The cold rotary forged samples showed higher YS due to relatively higher strain hardening, whereas higher ductility of the hot forged samples resulted in higher UTS. After heat treatment, the quenched and tempered martensite led to comparable stress–strain behavior and an increase in both YS and UTS values irrespective of the manufacturing routes. This was believed to be attributed to the grain refinement and subsequent increase in the hardness. Figure 20 summarizes the average YS and UTS values of three as-manufactured components before and after the heat treatment. The coarser grain structure and lower hardness of the as-machined sample led to significantly high YS and UTS than cold rotary forged sample. The heat treatment led to similar YS and UTS for both as-machined and cold forged samples, which

was attributed to their similar tempered martensitic microstructure and comparable hardness. The hot forged sample showed slightly different tensile behavior, *i.e.*, lowest YS but highest UTS, due to its higher ductility when compared to others. After heat treatment, a significant increase in YS but a minor increase in UTS was observed in the hot forged sample, which could be attributed to the refined microstructure, higher hardness and improved grain flow.

Figure 21 shows the fatigue properties of these as-manufactured components before and after heat treatment. The fatigue life of each test specimen was plotted in the S–N curve and then a trend (shown in dotted line) was identified for each manufacturing route to understand the change in fatigue behavior before and after the heat treatment. It should be noted that most of the fatigue specimens fractured before reaching to the fatigue cycle limit, however, few samples from the machining and hot forging process routes reached run-out (*i.e.*, discontinued when reached to fatigue cycle limit, indicated by black dotted circles). As expected, the heat treatment led to higher fatigue life for all three manufacturing routes due to microstructural refinement. After heat treatment, the as-machined sample showed highest fatigue life, which was closely followed by both hot forged and cold rotary forged samples. Particularly, the cold rotary forged sample showed substantially high fatigue strength (750 to 1000 MPa) with a significant improvement in fatigue life after heat treatment.

## IV. DISCUSSION

The suitability of both the hot forging and cold rotary forging routes was investigated to manufacture the flat cylindrical-shaped machine drive components in comparison with the current manufacturing route, *i.e.*, machining. Both as-machined and cold rotary forged

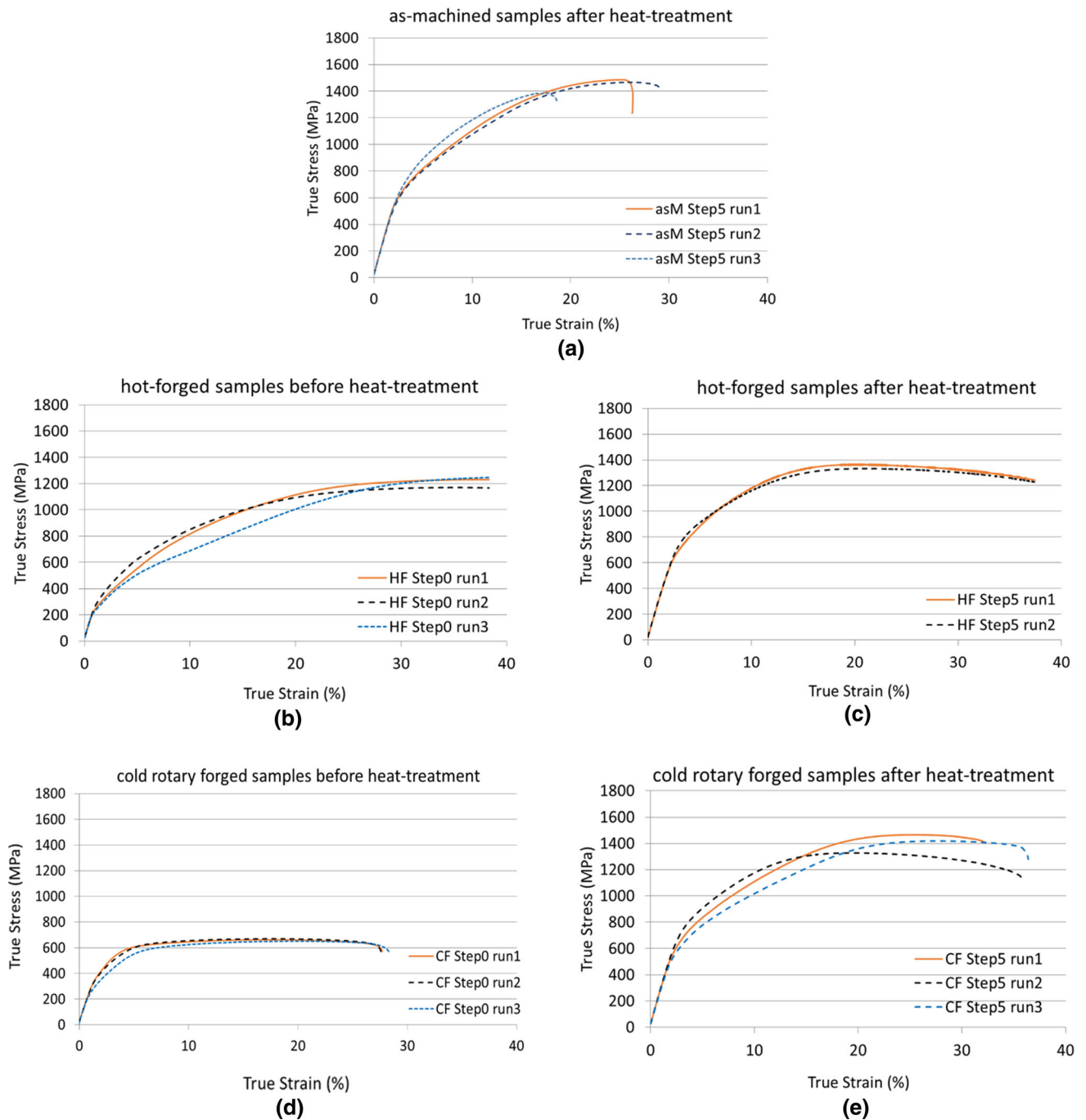


Fig. 19—Tensile behavior of (a) as-machined, (b, c) hot forged, and (d, e) cold rotary forged samples before and after heat treatment.

components showed an undesired banded pearlitic-ferritic microstructure, whereas the hot forged component showed a homogeneous bainitic-ferritic microstructure with no banding. An improvement in the grain flow with no trace of fracture was observed for both hot forged and cold rotary forged components as compared to the as-machined component. Due to different initial microstructures, the as-manufactured components (Step0) showed a significant difference in the average hardness values, deformation texture with variable texture strengths and average tensile strength. A

multi-step heat treatment was applied to the as-manufactured components in order to improve their microstructural and mechanical properties. The heat treatment combined two important steps—(i) hardening followed by oil quenching (Step3), which transformed any initial microstructure (such as pearlitic-ferritic and bainitic-ferritic) to the same acicular martensitic microstructure and (ii) tempering (Step5), which maintained the needle-like tempered martensitic microstructure with high hardness till the end. The cold rotary forging operation particularly improved the grain flow



- inferior mechanical properties as compared to the other two routes, whereas the hot forging exhibited homogeneous microstructure, higher hardness, and better fatigue properties among three routes.
- The optimized six-step heat treatment significantly improved the microstructural and mechanical properties of the cold rotary forged component when compared to the other two routes.
  - The cold rotary forging with the optimized heat treatment can be deemed as the best manufacturing route of the three routes investigated, due to its highest material utilization (which in turn saves significant cost), better microstructure and grain flow, high average hardness, tensile, and fatigue strength.

### ACKNOWLEDGMENTS

This work is a part of Innovate UK (I-UK) funded project ‘Supply Chain Optimization of Traction Drive Core Components Technology’ (S-CONTACCT, TSB Application Number 36553-255168). The authors would like to thank Gordon Gourley and Kyle Watt for manufacturing flat cylindrical-shaped machine drive components and Kornelia Kondziolka for metallurgical sample preparation.

### AUTHOR CONTRIBUTION

All authors contributed to the study conception and design of this work. Paranjayee Mandal, Maider Olasolo, and Laurie da Silva performed microstructural and mechanical experiments, data collection, and analysis. Himanshu Lalvani supervised and reviewed this work. Paranjayee Mandal wrote the first manuscript draft and all authors commented on the draft versions. All authors read and approved the final manuscript.

### OPEN ACCESS

This article is licensed under a Creative Commons Attribution 4.0 International License, which permits use, sharing, adaptation, distribution and reproduction in any medium or format, as long as you give appropriate credit to the original author(s) and the source, provide a link to the Creative Commons licence, and indicate if changes were made. The images or other third party material in this article are included in the article’s Creative Commons licence, unless indicated otherwise in a credit line to the material. If material is not included in the article’s Creative Commons licence and your intended use is not permitted by statutory regulation or exceeds the permitted use, you will need to obtain permission directly from the copyright holder. To view a copy of this licence, visit <http://creativecommons.org/licenses/by/4.0/>.

### REFERENCES

1. Steel and tube (2014). Case Hardening Steel—18CrNiMo7-6 or 17CrNiMo6. <http://stainless.steelandtube.co.nz/wp-content/uploads/2014/06/CaseHardeningSteel18CrNiMo7.pdf>.
2. International Molybdenum Association, IMO: *Case-Hardening Steel*. <http://www.imoa.info/molybdenum-uses/molybdenum-grade-alloy-steels-irons/case-hardening-steel.php>.
3. I.R. Mathesiusová and D.D.I.A. Kříž: *Metal*, 2012, vol. 5, pp. 23–25.
4. I.D. Verhoeven: *J. Mater. Eng. Perform.*, 2000, vol. 9, pp. 286–96.
5. Q.F. Wang, C.Y. Zhang, W.W. Xu, S.J. Zhao, X.Q. Zhao, and Z.S. Yan: *Proc. Sino-Swed. Struct. Mater. Symp.*, 2007.
6. Ovako: Material Data Sheet Steel Grade-18CrNiMo7-6, December 2017. [https://webcache.googleusercontent.com/search?q=cache:PW5X\\_f7mjBwJ:https://steelnavigator.ovako.com/steel-grades/18crnimo7-6/pdf%3FvariantIDs%3D330+%cd=4&hl=en&ct=clnk&gl=uk](https://webcache.googleusercontent.com/search?q=cache:PW5X_f7mjBwJ:https://steelnavigator.ovako.com/steel-grades/18crnimo7-6/pdf%3FvariantIDs%3D330+%cd=4&hl=en&ct=clnk&gl=uk).
7. Saarstahl: Material Specification Sheet-18CrNiMo7-6 (17CrNiMo6), 2016. <https://www.saarstahl.com/sag/downloads/download/11806>.
8. A. Ciski, T. Babul, and M. Duchek: *9th Youth Symp. Exp. Solid Mech.*, Trieste, Italy, July 2010.
9. P. Mandal, A.A. Mamun, L.D. Silva, H. Lalvani, M. Perez, and L. Muir: *Heat Treat 2017*, Columbus, OH, US, 2017.
10. Y. Prawoto, N. Jasmawati, and K. Sumeru: *J. Mater. Sci. Technol.*, 2012, vol. 28, pp. 461–66.
11. B. Białobrzeska, L. Konat, and R. Jasinski: *Metals*, 2017, vol. 7, pp. 1–20.
12. The Library of Manufacturing. [http://thelibraryofmanufacturing.com/forming\\_basics.html](http://thelibraryofmanufacturing.com/forming_basics.html).
13. Farinia Group: Cold Forged Parts Save Cost and Deliver Excellent Results, January 2020. <https://www.farinia.com/forge/cold-forging/cold-forged-parts-save-cost-and-deliver-excellent-results>.
14. SteelForging, CFS Machinery Co. Ltd.: Hot Forging vs. Cold Forging, 5 January 2018. <http://www.steelforging.org/hot-forging-vs-cold-forging/>.
15. Interplex Holdings Pte. Ltd.: Cold Forging Tech Bulletins. Advantages of Cold Forging vs. Machining, 2016. <https://interplex.com/app/uploads/Technical-Bulletin-Advantages-Cold-Forging-vs-Machining-Better-Strength-Productivity-Material-Savings-Design-Flexibility.pdf>.
16. S. Semiatin: *ASM Handbook: Metalworking: Bulk Forming*, ASM International, Materials Park, 2005, vol. 14A, pp. 179–82.
17. American Gear Manufacturers Association, AGMA: *AGMA 926-C99: Recommended Practice for Carburized Aerospace Gearing*, January 1999.
18. ASTM International: *Standard Test Methods for Determining Average Grain Size* (Designation: E112-13), 2013.
19. M.J. Roberts: *Metall. Trans.*, 1970, vol. 1, pp. 3287–94.
20. S. Morito, H. Yoshida, T. Maki, and X. Huang: *Mater. Sci. Eng. A*, 2016, vols. 438–440, pp. 237–40.
21. M. Yang, S.-L. Long, and Y.-L. Liang: *IOP Conf. Ser. Mater. Sci. Eng.*, 2018, vol. 324, p. 012043.
22. T. Maki: *Phase Transformations in Steels: Diffusionless Transformations High Strength Steels Modelling and Advanced Analytical Techniques*, Woodhead Publishing Series, Cambridge, 2012, pp. 34–58.
23. L. Ryde: *Mater. Sci. Technol.*, 2006, vol. 22, pp. 1297–1306.
24. F.J. Humphreys: *Scripta Mater.*, 2004, vol. 51, pp. 771–76.
25. ASTM International: *Standard Test Method for Knoop and Vickers Hardness of Materials* (Designation: E384-11), 2015.
26. Struers. <https://www.struers.com/en-GB/Knowledge/Hardness-testing/Vickers#>.
27. B. Roebuck, M. Brooks, and A. Pearce: *Good Practice Guide for Miniature ETMT Tests*. NPL Measurement Good Practice Guide No. 137, 2016.
28. Technical Committee ISO/TC 164: *Mechanical Testing of Metals, Subcommittee SC 5, Fatigue Testing (2010–11) Metallic Materials—Rotating Bar Bending Fatigue Testing* (ISO 1143:2010).
29. O. Sherby, J. Wadsworth, D. Lesuer, and C. Syn: *THERMEC 2006*, Vancouver, Canada, 2006.
30. S. Suwas and R.K. Ray: *Crystallographic Texture of Materials*, Springer, London, 2014, pp. 11–38.
31. K. Lücke and M. Hölscher: *Text. Microstruct.*, 1991, vols. 14–18, pp. 585–96.

**Publisher’s Note** Springer Nature remains neutral with regard to jurisdictional claims in published maps and institutional affiliations.